2004

Fabrication and Comprehensive Modeling of Ion-Exchanged Bragg Opitcal Add-Drop Multiplexers

Jose M. Castro
University of Arizona

David F. Geraghty
Unviersity of Arizona

Brian R. West
Wilfrid Laurier University, bwest@wlu.ca

Seppo Honkanen
University of Arizona

Fabrication and comprehensive modeling of ion-exchanged Bragg optical add–drop multiplexers

Jose M. Castro, David F. Geraghty, Brian R. West, and Seppo Honkanen

Optical add–drop multiplexers (OADMs) based on asymmetric Y branches and tilted gratings offer excellent-performance in wavelength-division multiplexed systems. To simplify waveguide fabrication, ion-exchange techniques appear to be an important option in photosensitive glasses. Optimum OADM performance depends on how accurately the waveguide fabrication process and tilted Bragg grating operation are understood and modeled. Results from fabrication and comprehensive modeling are compared for ion-exchange processes that use different angles of the tilted grating. The transmission and reflection spectra for the fabricated and simulated OADMs show excellent agreement. The OADM's performance is evaluated in terms of the measured characteristics of the Y branches and tilted gratings.

OCIS codes: 130.3120, 130.1750, 230.1480.

1. Introduction

Several filter technologies have been utilized to perform an add–drop operation optically in wavelength-division multiplexed systems. In recent years, designs that combine the operation of Y branches as mode splitters and tilted gratings as mode converters have been both demonstrated[1–3] and modeled.[4,5] Implementation of these optical add–drop multiplexers (OADMs) by ion-exchange techniques in photosensitive glasses has the potential of producing high-performance operation in a compact device with simple fabrication procedures. The performance of these devices can be evaluated in terms of the optical signal-to-noise ratio (OSNR) at drop and output ports. The OSNR, in turn, depends on the spectral transmission (or reflection) characteristics of the tilted grating and on the coupling parameters at the Y branch.[4,5]

The operation of a Bragg reflective OADM requires a flat and transparent transmission spectrum (0-dB loss) with a sharp dip at the wavelength to be dropped. This type of filter response can be obtained with a Bragg grating written normal to the waveguide. In that scheme, however, a circulator is required for physical separation of the dropped channel. A tilted Bragg grating written in the waist in which two single-mode asymmetric branches converge (Fig. 1) does not require additional components to separate incoming signals from the dropped signal.

The operation of the asymmetric Y branch with a tilted Bragg grating has been explained in detail elsewhere.[4–6] In an ideal asymmetric Y branch, channels from the narrower branch excite only the odd modes of the waist. Tilted gratings in the waist operate at three different Bragg conditions and can produce good coupling between odd–odd, odd–even, and even–even modes. However, there is an angle at which the tilted grating maximizes the desired odd–even mode conversion while it minimizes the odd–odd coupling.[4,5] At this angle, only the channel at the odd–even Bragg condition is reflected and dropped. This channel, traveling backward as an even mode, ideally will couple only to the wider branch. Using the second Y-branch, one can add one channel from the wider branch as it is coupled to the even mode of the waist and reflected with mode conversion to the narrow branch.

Several designs to improve the performance of the Y-branch Bragg OADM have been proposed. Accurate modeling of the fabrication process is necessary for effective implementation of these designs. To obtain the transmission characteristics of an OADM requires both grating and waveguide parameters.

J. M. Castro (jmcastro@email.arizona.edu) and D. F. Geraghty are with the Department of Electrical and Computer Engineering, The University of Arizona, 1230 East Speedway Avenue, Tucson, Arizona 85721-0104. B. R. West and S. Honkanen are with Optical Sciences Center, The University of Arizona, 1630 East University Boulevard, Tucson, Arizona 85721-0094.

Received 30 April 2004; revised manuscript received 23 August 2004; accepted 25 August 2004.

0003-6935/04/336166-08$15.00/0

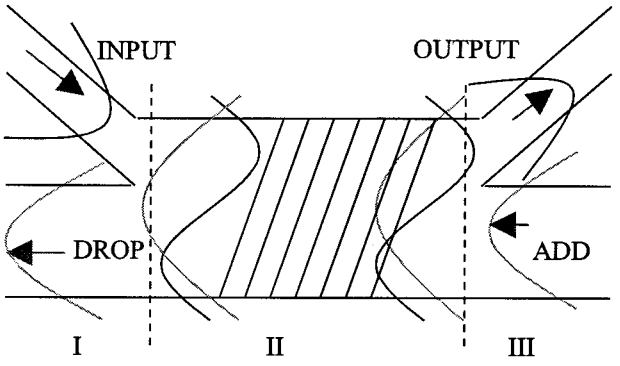

Fig. 1. Optical add–drop multiplexer: I, input Y branch; II, waist with tilted Bragg grating; III, output Y branch.

No direct comparison of designs and experiments has been made for these Y-branch Bragg OADMs. Making such a comparison is particularly difficult with Y-branch Bragg OADMs that use ion-exchanged waveguides, because accurate modeling of ion-exchanged waveguide index profiles is difficult. Only recently have advanced models that predict the ion concentration profiles with high enough accuracy been developed.[7] In the research reported in this paper, we apply our advanced model for ion-exchanged waveguides to design Y-branch Bragg OADMs. The modeling results are compared with measured data obtained from samples fabricated with buried ion-exchanged waveguides and photowritten gratings. We demonstrate excellent agreement between models and experiments. The possibility of predicting the performance of these OADMs accurately offers great promise for taking full advantage of the attractive features of buried ion-exchanged waveguides in photosensitive glasses.

2. Waveguide Fabrication

The samples were fabricated in the 2-mm-thick borosilicate glass BGG31 ($n = 1.4574$ at 1.55 μm) by Ag^+–Na^+ ion-exchange techniques. Two sets of samples were fabricated, as shown in Fig. 2. Set 1 consists of four double-sided asymmetric Y branches that converge into a two-mode waist. There are two branches as shown in Fig. 1, section I: the narrower and the wider branches and the waist in the mask are 2, 3, and 5 μm, respectively. Set 2 consists of two one-sided, nontilted Y-branch waveguides with dimensions similar to those of set 1. In the waist of the OADM of set 1 a Bragg grating was photowritten. In those waveguides the waist direction was tilted by a small angle with reference to the grating normal. The angle of tilt from the mask was 1°–4°.

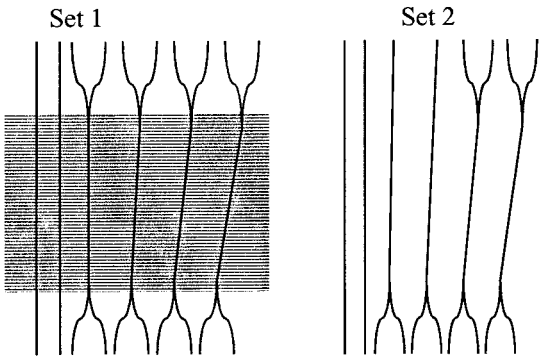

Fig. 2. Samples in set 1 (double-sided Y branch with tilted grating) and set 2 (single-sided Y branch). Arbitrary scale and position.

The first step in the fabrication of the waveguides was to coat the glass with a 100-nm-thick Ti mask, which was then patterned with the OADM design. Subsequently the mask was oxidized for 1 h in a sodium nitrate salt melt at 380 °C and then placed into a 1:1 $AgNO_3$:$NaNO_3$ melt at 280 °C for 1 hour. Next, the Ti mask was removed and a field-assisted burial of the waveguides was performed for 5 min at 275 V. Finally, the sample was cut and the end facets were polished.

The Bragg grating was photowritten by exposure of the glass for 12 min to 85 mJ of energy per pulse at 248 nm at a repetition rate of 50 Hz. The grating was 8 mm long by 2 mm wide; the grating provided adequate coverage for the waveguides in set 1. During photowriting, an angular alignment error (equal for all waveguides) estimated at ±0.5° was produced. The period of the grating was 535 nm (Λ_g), and the estimated index modulation (Δn) was 3.7×10^{-4}.

3. Ion Exchange and Waveguide Modeling

Fabrication of buried ion-exchanged waveguides consists of two steps: thermal diffusion and field-assisted burial. During diffusion, the exchange of ions of different sizes and polarizabilities produces a change in the refractive index near the surface of the glass. Both processes are described by the equation[8,9]

$$\frac{\partial C}{\partial t} = \frac{D_A}{1 - \alpha C}\left[\nabla^2 C + \frac{\alpha(\nabla C)^2}{1 - \alpha C} - \frac{e\mathbf{E}}{kT}\nabla C\right], \quad (1)$$

where C is the normalized concentration of the incoming dopant, D_A is its self-diffusion coefficient, e is the electron charge, k is Boltzmann's constant, T is the absolute temperature, $\mathbf{E}$ is the applied external electrical field, and α is defined as

$$\alpha = 1 - \frac{D_A}{D_B}, \quad (2)$$

where D_B is the self-diffusion coefficient of the outgoing ion. Both self-diffusion coefficients D_B and D_A depend on the composition and the temperature of the glass. An important property of our ion-exchange model is that it takes into account the effect of nonhomogeneous conductivity that results in a nonconstant electric field profile during the field-assisted burial step.[7] This effect is due to the different mobilities of the two ions, A and B (the incoming ion, silver, and the outgoing ion, sodium, in our case).

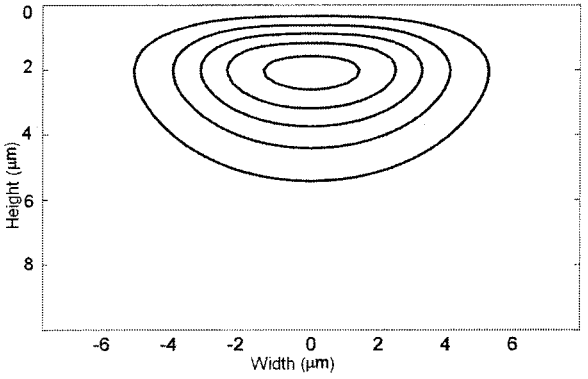

Fig. 3. Index profile after diffusion and burial. Contours at 0.1, 0.3, . . . , 0.9 of dn_{max}.

The local change in refractive-index profile is proportional to the concentration of ion A:

$$n(x, y, \lambda) = n_{sub}(\lambda) + dn_{max}(\lambda)C_A(x, y), \quad (3)$$

where $n_{sub}(\lambda)$ is the substrate index before ion exchange and $dn_{max}(\lambda)$ is the change in refractive index that results when $C_A = 1$, determined experimentally.

Electric field Ψ_m of each quasi-TE and -TM mode supported by the waveguide is found by solution of the Helmholtz equation

$$(\nabla^2 + k^2)\Psi_m = \beta_m{}^2\Psi_m, \quad (4)$$

where $k = k_0 n(x, y) = 2\pi n(x, y)/\lambda$ is the wave number and β_m is the propagation constant of the mth mode. We employ a semivectorial finite-difference method described in Ref. 10 to solve Eq. (4) with the appropriate discontinuity conditions of the normal field components.

4. Mode Profiles from Measurements and Modeling

From the model, Eqs. (1)–(3), and the fabrication parameters described in Section 3, the index profile of the waist was obtained as shown in Fig. 3. Using this index distribution, we obtained the mode profiles and effective indices of the even and odd modes of the OADM waist from a numerical solution of Eq. (4), as given in Table 1 and shown in Fig. 4.

To measure the intensity mode profiles of set 2 samples we used an input source of 1.55 μm and an IR camera with 256 gray-scale levels and 50 nm × 50 nm pixel resolution. The even-mode profile was obtained when the power was launched in the wider branch. We used the narrower branch as input to obtain the intensity profile of the odd mode.

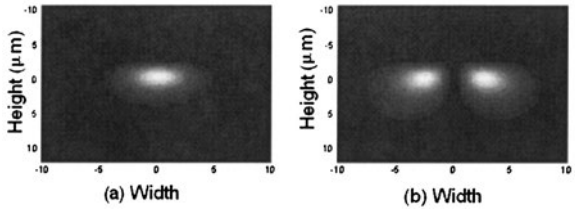

Fig. 4. Modeled intensity profiles: (a) even mode, (b) odd mode.

Figure 5 shows the measured even and odd intensity mode profiles. These small variations compared with the modeled profiles were attributed to temperature changes during fabrication or to small errors in lithographic precision.

5. Grating Modeling

Two-mode waveguides with a tilted grating can have three reflections: odd–even, odd–odd, and even–even. Each reflection is centered at a different wavelength and has a different strength and bandwidth. Although only the odd–even (or even–odd) reflection is required for performing the add–drop function, the strength of the other reflections that do not provide mode conversion can be reduced only for specific angles. The design of Bragg gratings is explained in great detail elsewhere.[11–13] In the case of a tilted grating in a two-mode waveguide, mode conversion will occur at wavelength λ_{oe} if the period in the propagation direction, Λ_z, is given by

$$\lambda_{oe} = \Lambda_z[n_{eff}(0) + n_{eff}(1)]. \quad (5)$$

The other wavelengths that satisfy the non-mode-conversion Bragg condition are

$$\lambda_{oo} = \lambda_{oe}\frac{2n_{eff}(1)}{[n_{eff}(0) + n_{eff}(1)]}, \quad (6)$$

$$\lambda_{ee} = \lambda_{oe}\frac{2n_{eff}(0)}{[n_{eff}(0) + n_{eff}(1)]}. \quad (7)$$

Table 1. Measured Characteristics of Add–Drop Devices

Variable	Unit	Source	Value				Precision
θ	deg	Measured	1	2	3	4	±0.5
λ_{oo}	nm	Measured	1560.974	1562.11	1563.212	1564.89	±0.03
λ_{oe}	nm	Measured	1563.432	1564.411	1565.709	1567.388	±0.03
λ_{ee}	nm	Measured	1565.989	1566.908	1568.187	1569.885	±0.03
$n_{eff,0}$		$\lambda_{ee}/(2\Lambda_z)$	1.4632	1.4633	1.4632	1.4632	$\pm 10^{-4}$
$n_{eff,1}$		$\lambda_{oo}/(2\Lambda_z)$	1.4585	1.4588	1.4586	1.4587	$\pm 10^{-4}$
Transmission dip (oo)	dB	Measured	16.8	1.2	15.6	5.7	±0.5
Transmission dip (oe)	dB	Measured	14.7	23	18	5.6	±0.5
Transmission dip (ee)	dB	Measured	31.7	24.1	15.8	1.6	±0.5

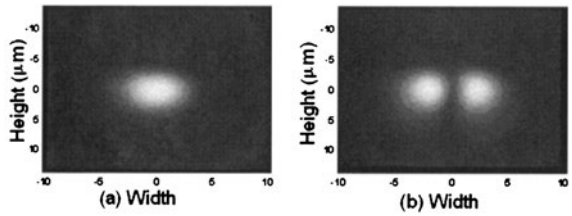

Fig. 5. Measured intensity profiles: (a) even mode, (b) odd mode.

The maximum reflection (transmission dip) at this wavelength is given by

$$R_{ab} = |r_{ab}|^2 = \tanh^2(\kappa_{ab} L), \tag{8}$$

where κ is the coupling coefficient, calculated as

$$\kappa = \frac{\pi}{\lambda} \Delta n \eta_{ab}(\theta). \tag{9}$$

In Eq. (9), λ and Δn are the free-space wavelength and the index modulation, respectively. The subscripts a and b represent odd and even modes, respectively, in the two-mode waveguide with the tilted grating, θ is the angle of the grating, and $\eta_{ab}(\theta)$ is the overlap integral[13]:

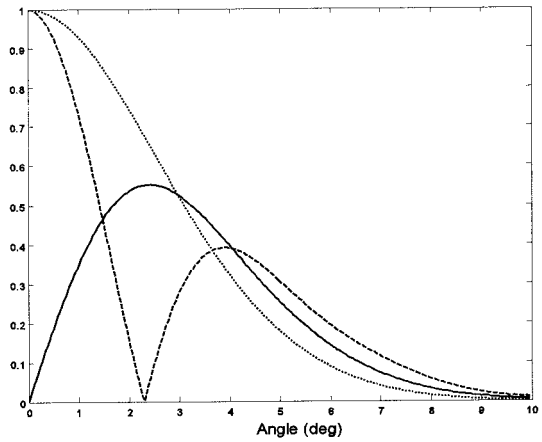

Fig. 6. Odd–odd (dashed curve), even–even (dotted curve), and odd–even (solid curve) overlap integrals as a function of the grating angle from modeled mode profiles.

$$\eta_{ab}(\theta) = \frac{\iint \Psi_a^*(x, y) \exp[i 2\pi x \tan(\theta)/\Lambda_z] \Psi_b(x, y) \mathrm{d}x\mathrm{d}y}{\left[\iint \Psi_a^*(x, y) \Psi_a(x, y) \mathrm{d}x\mathrm{d}y \iint \Psi_b^*(x, y) \Psi_b(x, y) \mathrm{d}x\mathrm{d}y\right]^{1/2}}. \tag{10}$$

The strength and the bandwidth of the three reflections depend on the index modulation, the grating length, and the overlap integral. However, there is only one factor that makes one property stronger than the other two: the overlap integral between modes in the tilted plane of the grating. The values of the overlap depend on the angle of the tilted grating, the index profile, the index difference, the waveguide width, and the grating period and width. To perform the add–drop function properly, one should tailor these variables to obtain maximum odd–even overlap integral while the odd–odd and even–even integrals are minimized.

Using Eq. (10), we obtained the values of the overlap integral for various angles of the tilted grating, as can be seen from Figs. 6 and 7 for the modeled process and the fabricated samples, respectively. In the latter case, the amplitude mode profiles were calculated from the measured power [$|\Psi_a(x, y)|^2$] of the modes. The even modes are symmetric, with constant phase across the mode profile. For the odd modes (antisymmetric) a π phase shift occurs laterally across the middle of the mode profile [Fig. 5(b)]. Figures 6 and 7 show that the odd–even overlap integral at 0° is zero because of the orthogonality of the modes, whereas the overlap between similar modes (odd–odd and even–even) is unity. The increase in the grating angle produces coupling between orthogonal modes owing to asymmetric perturbation. Therefore the odd–even overlap increases. For an angle near 2° the odd–odd overlap goes to zero and the odd–even overlap attains its maximum value. As a result, at this angle it is possible to obtain optimum performance for the OADM operation. Increasing the angle increases the odd–odd overlap and consequently the reflection of noise. It can be seen from

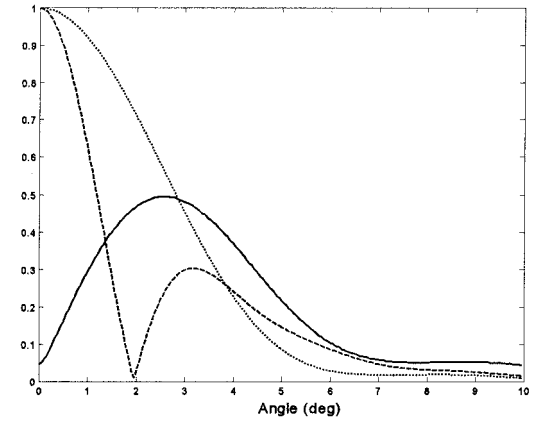

Fig. 7. Odd–odd (dashed curve), even–even (dotted curve), and odd–even (solid curve) overlap integrals as a function of the grating angle from measured mode profiles.

Figs. 6 and 7 that the even–even overlap is bigger than the odd–even overlap at the optimum angle; this will cause a large amount of even–even reflection. Nevertheless, the reflected power can be negligible because of mode rejection of the Y branch.[4–6] In practice, however, fabrication defects in the Y branch can lead to undesired coupling. The even mode traveling from the input port (narrow branch) can couple to odd and even modes (Cn_{eo}, Cn_{ee}) of the waist. In addition, the even mode from the add port (wide branch) can couple to odd and even modes (Cw_{eo}, Cw_{ee}) of the waist. From the waist, the even and odd modes can couple to even modes of the narrow and wide branches (Cn_{ee}, Cw_{ee}, Cn_{oe}, Cw_{oe}). The combined effect of the Y branch and the tilted grating in the OADM optical signal-to-noise ratio can be expressed as

$$\mathrm{OSNR}_{\mathrm{drop}} = 10 \log\left(\frac{Cn_{eo}R_{oe}Cw_{ee}}{Cn_{eo}R_{oo}Cw_{oe} + Cn_{ee}R_{ee}Cw_{ee}}\right), \tag{11}$$

$$\mathrm{OSNR}_{\mathrm{output}} = 10 \log\left[\frac{Cw_{ee}R_{oe}}{Cn_{eo}(1 - R_{oe})}\right]. \tag{12}$$

It can be seen from Eqs. (11) and (12) that to optimize the OADM it is necessary to minimize the mode cross talk (Cn_{ee}, Cw_{eo}) and the odd–odd reflection (R_{oo}) while maximizing Cn_{eo}, Cw_{ee}, and the reflection with mode conversation (R_{oe}).

6. Transmission Response from Modeling and Measurements

The transmission of the OADM was measured as a function of wavelength for the four angles of the tilted grating, and these results were compared with those predicted from modeling. To model the transmission spectrum we used two outputs from the waveguide model: the mode profiles and the effective indices. We used the transmission dips at the different Bragg conditions to estimate the angle that permits the maximum odd–even reflection while maintaining a low odd–odd reflection.

A. Transmission Spectra

TM transmission spectra for the four angles of the tilted grating of the OADM were measured with an erbium-doped fiber amplifier as a broadband source and an optical spectrum analyzer. As the transmission dips were convolved with the limited bandwidth of the optical spectrum analyzer (0.06 nm), they had to be measured again at the wavelengths of maximum reflection by use of a tunable laser and a photodetector. When power was launched and measured in the two opposite narrow branches (input and output port) of the OADM, two transmission dips were observed. One dip represents the odd–even reflection with mode conversion that is necessary to drop the channel and the other represents the unwanted odd–odd reflection. The transmission spectra are shown as dashed curves in Figs. 8(a), 9(a), 10(a), and 11(a).

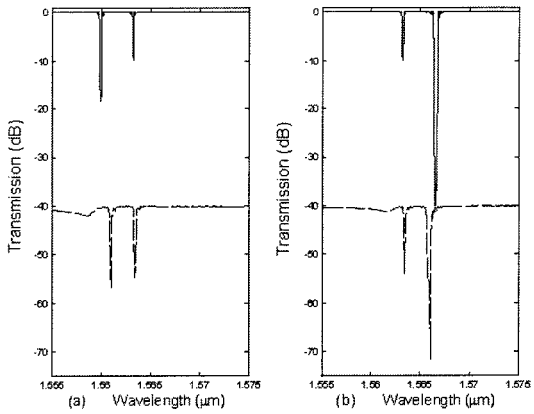

Fig. 8. Transmission at the first angle from complete simulation (solid curves) and from measurements (dashed curves, shifted by −40 dB). Power launched and detected (a) at the narrow branches and (b) at the wider branches.

On launching and measuring the power in the two opposite wide branches (drop and add ports) of the OADM, we again observed two transmission dips. In this case they represent the unwanted even–even reflection and again the desired odd–even reflection with mode conversion. The transmission curves are shown as dashed curves in Figs. 8(b), 9(b), 10(b), and 11(b). We obtained cross talk between modes at the Y-branch transition by launching and measuring the power at opposite branches that have different widths. The average value of this mode optical cross talk was approximately 20 dB.

The transmission responses from modeling were obtained by use of the overlap integrals and effective indices that were both computed (complete model) and measured. In the first case the solid curves in Figs. 8(a), 9(a), 10(a), and 11(a) represent the transmission response when the power was launched and measured in the narrow branches. Figures 8(b), 9(b), 10(b), and 11(b) show the transmission responses when the power was launched and measured

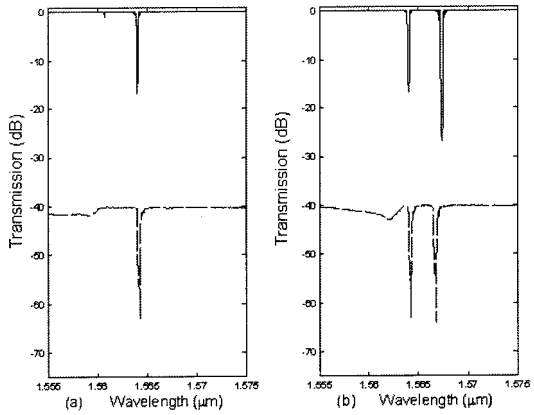

Fig. 9. Transmission at the second angle from complete simulation (solid curves) and from measurements (dashed curves, shifted by −40 dB). Power launched and detected (a) at the narrow branches and (b) at the wider branches.

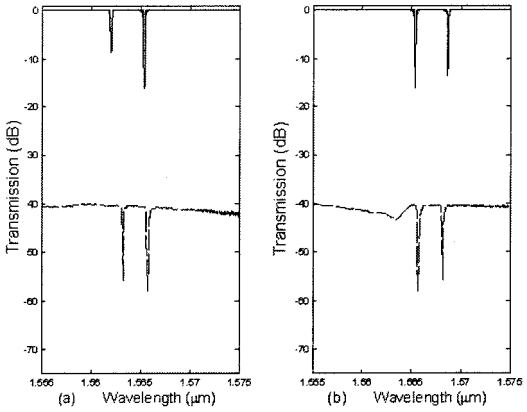

Fig. 10. Transmission at the third angle from complete simulation (solid curves) and from measurements (dashed curves, shifted by −40 dB). Power launched and detected (a) at the narrow branches and (b) at the wider branches.

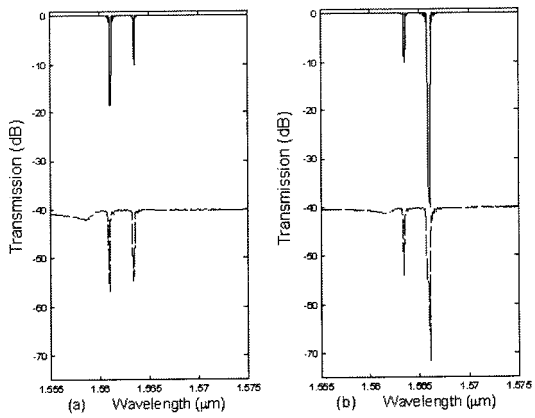

Fig. 12. Transmission at the first angle from partial simulation (solid curves) and from measurements (dashed curves, shifted by −40 dB). Power launched and detected (a) at the narrow branches and (b) at the wider branches.

in the wider branches. It can be seen from these figures that the Bragg wavelengths from modeling were slightly shorter in all cases. These differences (<2 nm), as well as the fact that the modeled mode profiles were wider than the measured profiles, were an indication that the effective indices were higher than the estimated indices. More-accurate values for the effective indices were obtained by use of the measured Bragg wavelengths and the period of the grating in the propagation direction as listed in rows 5 and 6 of Table 1.

The precision of the effective index calculation from measurements depends on the precision with which the optical spectrum analyzer measures wavelengths (±0.03 nm) and on the uncertainty in the grating period. The estimated error in the effective index measurements was $\pm 10^{-4}$: 1.4632 and 1.4637, respectively, for measured and modeled effective index $n_{\mathrm{eff},0}$ and 1.4586 and 1.4575 for measured and modeled effective index $n_{\mathrm{eff},1}$.

The average effective index of each mode was compared with this ion-exchange model. The error in the modeled effective index was less than 0.05%. We used the effective indices from the Bragg wavelengths as well as the overlap integral from measurements to obtain the transmission responses of the grating as shown by the solid curves in Figs. 12 and 13. In the same figures the measured transmission responses were plotted again (dashed curves) to make comparisons easy.

The transmission spectrum at the first angle (≈1°) when the power was launched and measured in the wider branches [Figs. 8(b) and 12(b)] shows that the even–even reflection (dashed curves at 1.5659 μm) is greater than the odd–even reflection (at 1.5634 μm). When the power was launched and measured in the narrower branches [Figs. 8(a) and 12(a)] the odd–odd reflection (at 1.5607 μm) was also greater than the odd–even reflections. Results from the models shown as solid curves show good agreement in both cases.

At the second angle (≈2°), when the power was

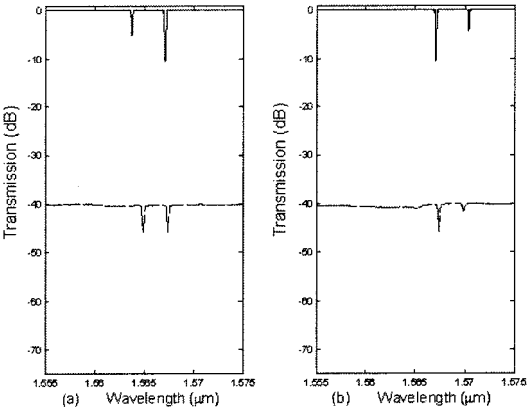

Fig. 11. Transmission at the fourth angle from complete simulation (solid curves) and from measurements (dashed curves, shifted by −40 dB). Power launched and detected (a) at the narrow branches and (b) at the wider branches.

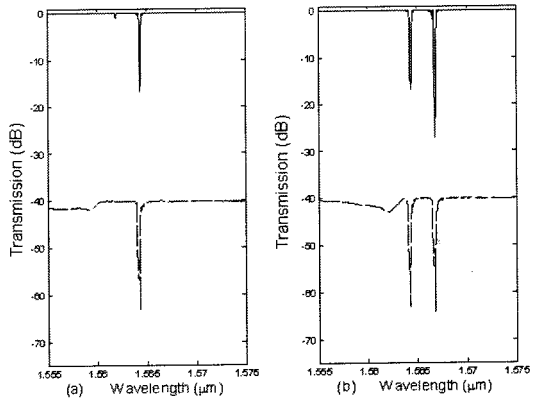

Fig. 13. Transmission at the second angle from partial simulation (solid curves) and from measurements (dashed curves, shifted by −40 dB). Power launched and detected (a) at the narrow branches and (b) at the wider branches.

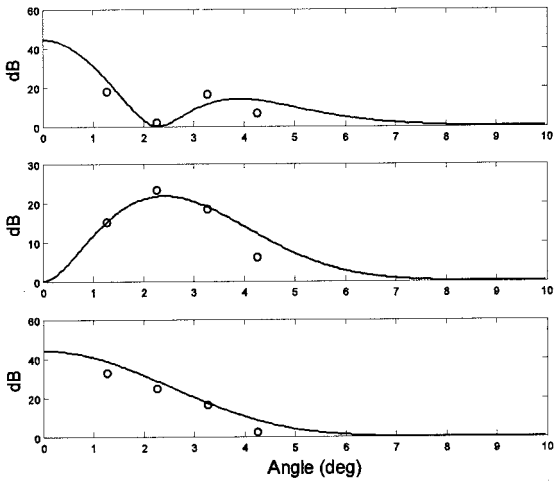

Fig. 14. Transmission dips for top, even–even; middle, odd–even; and bottom, odd–odd reflection. Solid curves and circles show transmission dips from the complete model and from measurements, respectively.

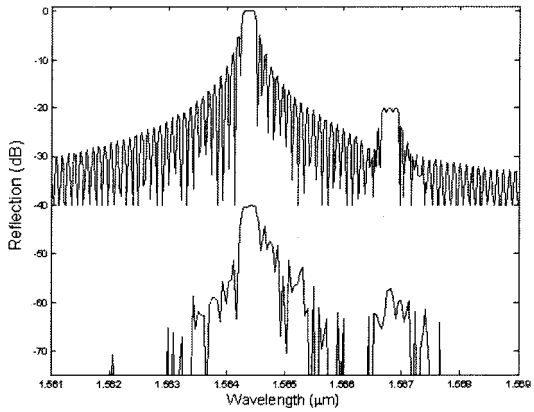

Fig. 15. Spectrum from simulation (solid curves) and measurements (solid curves, shifted by −40 dB) at the drop port. The power is launched from the input port.

launched in the narrow branch a maximum value for the odd–even reflection was found as expected from the model [Figs. 9(a) and 13(a)]. In the same figures a slight dip near 1.56 μm could be observed in the measured transmission owing to cladding modes. At the same angle, the even–even reflection was very strong, as shown in Figs. 9(b) and 9(b). At higher angles, results from the model and measurements showed decreases of reflections strength, as expected from their overlap integrals.

Another predictable effect from modeling was the increase in the wavelengths of maximum reflection (λ_{oo}, λ_{oe}, λ_{ee}) when the grating angle was increased. These increments were found to be proportional to the changes in the grating period in the propagating direction ($\Lambda_z = \Lambda_g/\cos\theta$). In all cases the transmission spectrum showed excellent agreement with the results of the model. In particular, when the overlap integrals and effective indices from measurements were used in the model, the differences between measurement and model were remarkably small.

B. Transmission Dips As a Function of Grating Angle

Transmission dips were obtained from modeling and measurements. As we mentioned above, the angles of the four OADMs relative to one another were accurately defined by mask lithography; however, the alignment of the Bragg grating to the sample would have provided an error in angle that was constant across all four OADMs, as the grating was simultaneously written for all of them. To improve the match between measured and modeled transmission dips we reduced the uncertainty that was due to angular misalignment (±0.5°) by matching the Bragg conditions of different angles and types of reflection:

$$n_{\text{eff}}\Lambda_g = \lambda^{(1)}\cos(1+\varepsilon) = \lambda^{(2)}\cos(2+\varepsilon) = \lambda^{(3)}\cos(3+\varepsilon) = \lambda^{(4)}\cos(4+\varepsilon), \quad (13)$$

where $\lambda^{(1)}$, $\lambda(2)$, $\lambda(3)$, and $\lambda^{(4)}$ are the measured wavelengths in the Bragg condition at the four angles and ϵ is the unknown shift that is common to all angles. As the grating period (Λ_g) and the width are the same for the four waveguides, the effective index was assumed equal for each. Under this assumption, a numerical solution for $\epsilon = 0.265$ was obtained with an uncertainty of $<0.1°$.

Figure 14 shows the transmission dips from the model presented in Sections 2 and 5 (solid curves) and from measurements (circles). From this figure it can be seen that the theoretical transmission dips as a function of angle agree with the measured values when the angular correction is made. From modeling and measurements, the operation of the OADM can be improved by use of a grating angle of ≈2.2°. At this angle the output port shows a flat spectrum with only one transmission dip, at λ_{oe}, when power is launched at the input port [Figs. 9(a) and 13(a)]. This indicates that the odd–even reflection necessary for performing the add–drop function is maximized at the drop port. The spectrum at this port, nevertheless, can also be affected by the power coupled from the input port as an even mode (Cn_{ee}). A second reflection peak (R_{ee}) appears in the spectrum, as shown in Figs. 9(b) and 13(b). This reflection peak is comparable with R_{oe}. However, the effect on the OSNR will depend on the magnitude of the even–even coupling (Cn_{ee}), as shown in Fig. 11. In the fabricated samples the cross talk limits the even–even peak 20 dB below the odd–even peak, as can be seen from measurements and modeling (Fig. 15).

7. Discussion and Summary

The modeled and measured transmission dips show excellent agreement in magnitude, wavelength, and angle position. The grating angle for maximum reflection with mode conversion is almost the same as the angle of minimum odd–odd reflection, as expected from the model.

The small errors in the results of the model are due primarily to the short time of burial: Because this

time is short, the effective duration of activity at the appropriate temperature might differ from the one used in the model. This uncertainty can explain the small discrepancies in the modeled and measured mode profiles and therefore in their overlap integrals. However, other reasons such as mode cross-coupling noise should also be considered.

The relationship between the transmission dips and performance parameters such as optical signal-to-noise ratio (OSNR) was described in Refs. 11 and 12. A simple estimation of the OSNR from the transmission dip between odd and even modes gave a value of $\sim$25 dB at the output port. Because of mode cross talk (Cn_{ee}), the OSNR at the drop port will be $\approx$20 dB. One can improve the OSNR at output by increasing the strength of the grating while maintaining the bandwidth. To do so requires an increase in the grating length and in the value of Δn. The OSNR at the drop port, however, can be improved by reduction of the mode cross talk at the asymmetric Y branch. It is clear that further improvements could be obtained by use of additional filters; simplicity, one of the main advantages of this type of OADM, would then be lost, however.

Another aspect to consider in this type of optical add–drop multiplexer is its polarization dependence (PD). In the measured samples a PD of 0.25 nm was found. The cause of that PD was attributed to some asymmetry in the index profile of the waveguide. Our measurements show no indication that the reflection strength is affected by the polarization of the source. Only a shift in the Bragg wavelengths were found, as expected from our waveguide modeling. Consequently we believe that the PD can be reduced by a deeper burial, postannealing,[14] or both.

In summary, ion-exchanged asymmetric Y-branch OADMs were proposed and demonstrated at acceptable levels of performance. Their comparative advantages lie in their compactness and their relatively simple fabrication procedure. To improve this type of OADM effectively will require control of the fabrication process. Modeling the process from input manufacturing parameters, such as voltage and temperature, to the final device characteristics, such as transmission response, is a main step in obtaining the desired control. In this paper we have shown that it is possible to model the operation of an OADM with an excellent degree of accuracy. Two ways to obtain the transmission characteristics of the device were presented. The first procedure predicted the transmission dips from the overlap integrals obtained from measured odd- and even-mode profiles at the waist. The second procedure produced the same transmission characteristics, but it used a complete model that began with the primary parameters of the ion-exchange process. The main sources of error were described: angular errors during fabrication, noise in the mode profile measurements, and mode cross talk at the Y branch. The interrelation of diverse theories such as ion exchange kinetics, wave equations, and coupled-mode theory have proved to be effective for modeling this device, as can be inferred from the remarkable agreement of theory with measurements.

The authors thank the Office of the Vice President for Research and Graduate Studies of the University of Arizona for funding in support of this research.

References

1. A. S. Kewitsch, G. A. Rakuljic, P. A. Willems, and A. Yariv, "All-fiber zero-insertion-loss add–drop filter for wavelength-division multiplexing," Opt. Lett. **23,** 106–108 (1998).
2. C. K. Madsen, T. A. Strasser, M. A. Milbrodt, C. H. Henry, A. C. Bruce, and J. Demarco, "Planar waveguide add/drop filter employing a mode converting grating in an adiabatic coupler," in *Integrated Photonics Research*, Vol. 4 of 1998 OSA Technical Digest Series (Optical Society of America, Washington, D.C., 1998), pp. 102–104.
3. D. F. Geraghty, D. Provenzano, M. M. Morrell, S. Honkanen, A. Yariv, and N. Peyghambarian, "Ion-exchanged waveguide add/drop filter," Electron. Lett. **37,** 829–831 (2001).
4. C. Riziotis and M. N. Zervas, "Design considerations in optical add/drop multiplexers based on grating-assisted null couplers," J. Lightwave Technol. **19,** 92–104 (2001).
5. C. Riziotis and M. N. Zervas, "Novel full-cycle-coupler-based optical add–drop multiplexer and performance characteristics at 40-Gb/s WDM networks," J. Lightwave Technol. **21,** 1828–1837 (2003).
6. T. Erdogan, "Optical add–drop multiplexer based on an asymmetric Bragg coupler," Opt. Commun. **157,** 249–264 (1998).
7. P. Madasamy, B. R. West, M. M. Morrell, D. F. Geraghty, S. Honkanen, and N. Peyghambarian, "Buried ion-exchanged glass waveguides: burial-depth dependence on the waveguide width," Opt. Lett. **28,** 1132–1134 (2003).
8. A. Tervonen, "Theoretical analysis of ion-exchanged glass waveguides," in *Introduction to Glass Integrated Optics*, S. I. Najafi, ed. (Artech House, Norwood, Mass., 1992), pp. 73–83.
9. R. V. Ramaswamy and R. Srivastava, "Ion-exchanged glass waveguides: a review," J. Lightwave Technol. **6,** 984–1000 (1988).
10. C. M. Kim and R. V. Ramaswamy, "Modeling of graded-index channel waveguides using nonuniform finite difference method," J. Lightwave Technol. **7,** 1581–1589 (1989).
11. R. Kashyap, *Fiber Bragg Gratings* (Academic, San Diego, Calif., 1999).
12. K. S. Lee and T. Erdogan, "Fiber mode coupling in transmissive and reflective fiber gratings," Appl. Opt. **39,** 1394–1404 (2000).
13. T. Erdogan and J. E. Sipe, "Tilted fiber phase gratings," J. Opt. Soc. Am. A **13,** 296–313 (1996).
14. D. F. Geraghty, D. Provenzano, M. M. Morrell, J. Ingenhoff, B. Drapp, S. Honkanen, A. Yariv, and N. Peyghambarian, "Polarisation-independent Bragg gratings in ion-exchanged glass channel waveguides," Electron. Lett. **36,** 531–532 (2000).